ACS Sustainable Chemistry & Engineering

Research Article

Ultrasonic Spray Nozzle-Mediated Green Activation for Hierarchical Pore-Structured Carbon Beads

Michael Hough, Artur Deditius, Neil Robinson, Gerd Elmar Schröder-Turk, Jacob Judas Kain Kirkensgaard, Volodymyr M. Gun'ko, Alexander V. Neimark, Katsumi Kaneko, and Piotr Kowalczyk*

Cite This: https://doi.org/10.1021/acssuschemeng.3c04171

Read Online

ACCESS | Metrics & More | Article Recommendations | Supporting Information

ABSTRACT: This study focuses on enhancing sustainability through energy-efficient methods in producing hierarchically structured porous carbons. A novel approach, utilizing an ultrasonic spray nozzle-quartz tube reactor (USN-QTR), is introduced for fabricating carbon beads with customizable ultra-, super-, and mesopores. This study showcases noteworthy results from subjecting spherical char particles to activation processes involving carbon dioxide, a mixture of carbon dioxide and micron-sized water droplets, and highly concentrated supercritical steam at a temperature of 1173 K for durations of 3 and 5 h. Through pulse-field gradient nuclear magnetic resonance measurements, it was noted that carbon beads produced using USN-generated highly concentrated supercritical steam displayed remarkably elevated intra-bead self-diffusivity of n-hexane. Inductively coupled plasma-optical emission spectroscopy demonstrates superior gold recovery kinetics from cyanide solutions compared to that from an industrial benchmark. The energy expenditure for USN-generated steam, producing carbon beads with an apparent surface area of 2691 m^2/g, is estimated at 97 J per 1 m^2 of carbon. This contrasts with the traditional steam generation method requiring approximately the energy of 190 J/m^2 for activated carbon with an S_{BET} of 2130 m^2/g, making the USN-assisted activation method a more environmentally friendly and sustainable option with nearly half the energy consumption.

KEYWORDS: Energy management, ultrasonic spray nozzle, steam activation, hierarchically porous carbon beads, pulse-field gradient nuclear magnetic resonance, small-angle X-ray scattering

INTRODUCTION

Nanoporous carbons have been widely and predominantly applied to green technologies.[1−10] One of the critical challenges in the production of nanoporous carbons is to achieve high-quality nanoporous carbons while minimizing energy consumption. The traditional energy-intensive activation methods do not align well with green technology.[11,12] It is necessary to innovate the production of nanoporous carbons having customized characteristics with less energy. One promising approach to achieve this is by leveraging the capabilities of an ultrasonic spray nozzle (USN), which has the potential to produce high-quality carbons while reducing energy consumption.

USN technology is an emerging technology that has found extensive applications in various fields, including spray coating, fabrication of nanoparticles, and synthesis of functional nanomaterials and catalysts.[13−18] A USN is a low-power consumption device that operates by converting high-frequency standing waves into mechanical energy, which is then transferred into a liquid. USN technology has the potential to accelerate and

precisely control the activation process of char. This is achieved by generating highly concentrated supercritical steam with uniform micrometer-sized droplets, which are sprayed directly into a quartz tube reactor without the need for a carrier gas. This innovative approach can lead to the production of high-quality nanoporous carbons. The use of USN-aided activation offers significant advantages over traditional char activation that relies on a water-heating process conducted outside a reactor to produce steam. The steam is subsequently combined with a carrier gas through a bubbling process and transported to the reactor.[11] The need to sustain high temperatures for the steam entails additional energy consumption to operate ribbon heaters

A

Table 1. Activation Parameters Used for the Production of HPSCBs[a]

Sample	Activation method and parameters	Burn-off (wt %)	Yield (wt %)
HPSCB-CO$_2$-3h	CO$_2$, 1173 K for 3 hours, ~2.0 dm^3/min	19 ± 0.7	15 ± 0.11
HPSCB-CO$_2$/H$_2$O-3h	Ultrasonically generated mist of uniform 18 μm water droplets sprayed to CO$_2$ (~2.0 dm^3/min), 1173 K, for 3 hours	31 ± 3.4	12 ± 0.10
HPSCB-H$_2$O-3h	**Ultrasonically generated mist of uniform 18 μm water droplets sprayed to the quartz tube reactor, 1173 K, for 3 hours**	**48 ± 2.5**	**9 ± 0.08**
HPSCB-CO$_2$-5h	CO$_2$, 1173 K for 5 hours, ~2.0 dm^3/min	24 ± 1.6	14 ± 0.06
HPSCB-CO$_2$/H$_2$O-5h	Ultrasonically generated mist of uniform 18 μm water droplets sprayed to CO$_2$ (~2.0 dm^3/min), 1173 K, for 5 hours	47 ± 2.7	9 ± 0.07
HPSCB-H$_2$O-5h	**Ultrasonically generated mist of uniform 18 μm water droplets sprayed to the quartz tube reactor, 1173 K, for 5 hours**	**79 ± 10.9**	**4 ± 0.09**

[a]The burn-off was determined using the sample weights before and after activation. The production yield was calculated by comparing the weight of the dry precursor sample to the weight of the dry carbon sample. The error in the burn-off degree and production yield is calculated as the standard deviation derived from three repeated experiments.
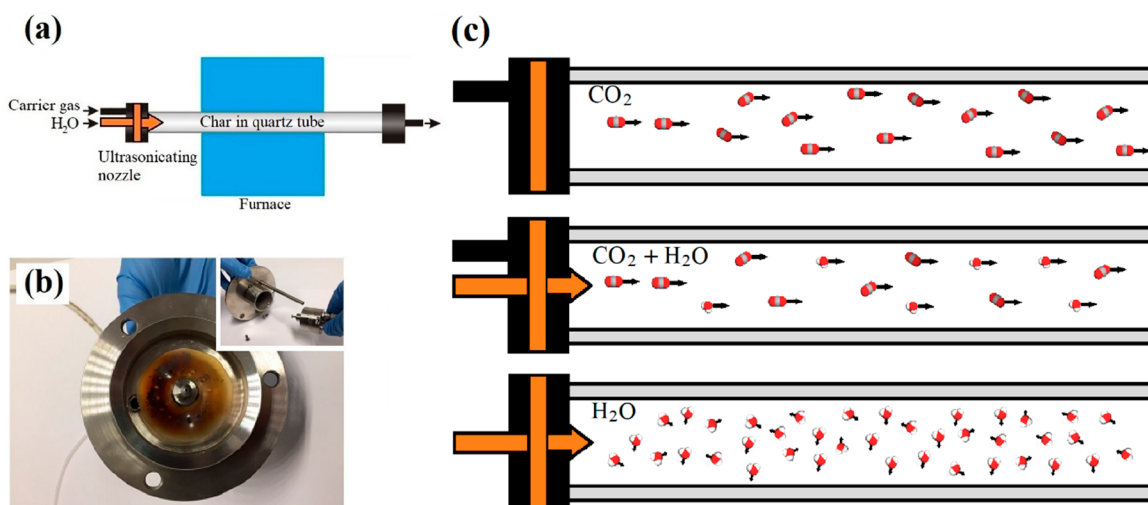
Figure 1. Scheme of the ultrasonic spray nozzle-quartz tube reactor (USN-QTR) used for the activation processes (a). An ultrasonic cone-shaped 120 kHz spray nozzle is incorporated into a stainless-steel sealing flange of the furnace; a nylon baffle distributes the carrier gas flow over the ultrasonic spray nozzle (b). Panel (c) provides a schematic diagram illustrating the activation of char using three different methods: CO$_2$ activation (top panel), CO$_2$ with ultrasonically sprayed micrometer-sized water droplet activation (middle panel), and highly concentrated supercritical steam activation without the use of a carrier gas (bottom panel).

or heating tapes. Moreover, the utilization of USN-aided activation is suitable for producing nanoporous carbons with customized pore structures, including hierarchical nanoporous activated carbons.[19,20] As far as we are aware, the integration of a USN into char activation processes has not been explored in previous research.

Hierarchical pore-structured carbon beads produced from ion-exchange resin beads possess numerous advantageous characteristics that make them highly suitable for a wide range of applications. These advantages include high level of chemical purity, good fluidity and packaging, a smooth outer surface topology, high mechanical strength, resistance to abrasion and dust formation, and the ability to customize surface area and porosity to meet specific requirments.[20,21] These applications encompass a broad range of uses and are not restricted to extracorporeal detoxification, hemo- and enterosorption, alleviating chemotherapy side effects, extracting precious metals from low-grade ore through adsorption from cyanide solutions, and catalyst support.[20−27] To ensure both high chemical purity and precise control over the hierarchical pore structure of carbon beads, it is crucial to develop and construct innovative reactors for char activation that eliminate the requirement for external chemical activating agents. To improve both energy and

water efficiency in the activation process that utilizes steam, it is imperative to reduce the costs associated with steam production and its transportation. This can be achieved by adopting state-of-the-art USN technology, which offers a promising solution for cost reduction without compromising the steam utilization performance.

In this study, we developed and built an ultrasonic spray nozzle-quartz tube reactor (USN-QTR) for char activation. We applied the USN-QTR to produce two series of hierarchical pore-structured carbon beads (HPSCBs) through activation processes lasting 3 and 5 h. These processes included CO$_2$ activation, ultrasonically generated micron-sized water droplets injected with CO$_2$ activation, and highly concentrated supercritical steam activation without the use of a carrier gas (Table 1 and Figure 1). The impact of alterations in accessible and inaccessible pore volume and surface area fractions, pore size distributions, and intrabead self-diffusivity of *n*-hexane is examined through high-resolution nitrogen adsorption, small- and wide-angle X-ray scattering, and pulse-field gradient nuclear magnetic resonance spectroscopy. In the context of an industrially relevant problem, we have examined the impact of USN-assisted activation on the kinetics of gold dicyanide recovery. This investigation was conducted using inductively

coupled plasma-optical emission spectroscopy (ICP-OES). The energy cost of steam generation using a USN and water heating for the production of 1 m² of the apparent BET surface area has been estimated and thoroughly discussed.

■ EXPERIMENTAL SECTION

Synthesis. HPSCBs were prepared through a two-step activation process, with carbonization performed as a separate step followed by activation. The carbon precursor employed consisted of beads of an acidic, macroporous cation exchange resin synthesized from a styrene-divinylbenzene copolymer (mean bead size = 670 ± 50 μm, S_{BET} = 15 m²/g, V_p = 0.144 cm³/g, and an average pore size D = 32.72 nm) and supplied by Lewatit MonoPlus SP 112 H, Lanxess Pty Ltd. (Germany). High-purity N_2 and CO_2 gases were procured from BOC Gas (Australia). The Reverse Osmosis (4 stages, IBIS Technology, Australia) and Milli-Q Reference Water Purification System were used to produce deionized water (18.2 MΩ·cm at 25 °C).

The carbonization process involved taking approximately 2 grams of the polymeric precursor and placing it in a ceramic crucible. The crucible containing the sample was placed into a reactor and then heated to a temperature of 803 K for a duration of 2 hours. Nitrogen gas was employed as a carrier gas at a flow rate of around 2.0 dm³/min (Figure 1(a)). The result of this carbonization process was approximately 82% weight-loss of the precursor, which was determined by measuring the sample's weight before and after carbonization. Following carbonization, approximately 1 g of the resulting char was subjected to the activation process. The activation method and specific parameters used can be found in Table 1 and are schematically shown in Figure 1.

An ultrasonic cone-shaped spray nozzle operating at 120 kHz (Sono-Tek Corp., USA) and set to a constant power of 3.0 W was employed for the generation of micrometer-sized water droplets (Figure 1(b)). Deionized water was delivered at a constant flow rate of 0.2 cm³/min through a Teflon tube measuring 0.45 m in length with an inner diameter 0.96 mm, facilitated by a syringe pump. It is important to note that the activation process with highly concentrated supercritical steam was accomplished by continually injecting water droplets generated by the USN directly into the quartz tube reactor without the need for a carrier gas flow (see movies in the Supporting Information). The concentration of supercritical steam was gradually increased in a controlled manner over 3 and 5 h, as illustrated in the bottom panel of Figure 1(c). After 5 h of activation at 1173 K, the estimated density of supercritical steam within the quartz tube reactor is approximately 0.031 g/cm³.

Low-Temperature Nitrogen Adsorption and Scanning Electron Microscopy. The porosity of both the char and HPSCBs was evaluated by using nitrogen adsorption−desorption isotherms at 77 K (Tristar II 3020, Micromeritics, USA). Prior to the measurements, the samples were subject to vacuum degassing at 473 K for 24 h. The pore size distributions (PSDs) and textural characteristics were assessed using the quenched solid density functional theory (QSDFT) method.[28−30] A mixed slit and cylindrical kernel was used to model equilibrium nitrogen adsorption in micro- and mesopores, respectively.[28−30] The apparent Brunauer−Emmett−Teller (BET) surface areas were determined by analyzing the nitrogen adsorption isotherms within a relative pressure range of 0.05−0.3 (Table S1). Scanning electron microscopy (SEM) observations and the energy-dispersive X-ray (EDX) analyses of carbon samples were conducted using a Verios XHR SEM system at the Centre for Microscopy, Characterization, and Analysis (CMCA) at the UWA. A slow-curing transparent epoxy known as EpoFix was prepared by combining the resin and hardener in a weight ratio of 25:3, respectively. Subsequently, carbon beads were introduced into a 25 mm diameter mounting cup named FixiForm along with the epoxy. The combined mixture was subjected to a vacuum within a desiccator for a minimum duration of 24 h. Following this, the epoxy molds containing the carbon beads underwent a polishing process to reveal the interior of the beads. Subsequently, they were coated with carbon before being imaged by SEM.

Small-Angle and Wide-Angle X-ray Scattering Measurements. Combined small-angle X-ray scattering (SAXS) and wide-angle X-ray scattering (WAXS) patterns were collected using a Nano-inXider instrument from Xenocs SAS (Grenoble, France) with Cu Kα radiation and a two-detector setup for simultaneous measurements of the SAXS and WAXS. Both detectors are Pilatus 300 k pixel detectors from Dectris (Baden, Switzerland). The scattering intensity is a function of the wavevector magnitude $q = 4\pi \sin(\theta)/\lambda$, with a specific value of X-ray wavelength λ = 0.154 nm being used in this study. The samples were loaded into vacuum-tight containers and sealed with 5−7 μm thick mica windows. Each measurement was conducted under a vacuum, with an acquisition time of 60 min. Standard reduction software (XSACT) was used to average and correct the two-dimensional scattering data to yield the data curves. The 1D SAXS and WAXS data were merged into a single scattering curve, and the background from the mica windows was subtracted (Figure S1). The theoretical treatment of the SAXS data is described in detail in Supporting Information, Section 1. The standard X-ray scattering diffraction analysis was conducted using a Rigaku SmartLab instrument equipped with a HyPix-3000 detector. The X-ray source used was Cu Kα with a wavelength of 0.154 nm. The analysis covered the angular range 10−90° (2θ) with a step of 0.01° (2θ) and a scanning speed of 4°/min. A silicon zero diffraction holder was used for the measurements (Figure S2). The spacing between the graphite layers was determined using the Bragg equation[31] (Table S1).

PFG NMR Diffusion Measurements. For NMR diffusion analysis, the samples were prepared by immersing ~1.5 g in excess *n*-hexane (>98%, Sigma-Aldrich). These samples were sealed tightly in 5 mm NMR tubes (Bruker BioSpin) and left to soak for a minimum of 48 h. The ¹H pulsed-field gradient (PFG) NMR measurements were conducted by using a Magritek Spinsolve Diffusion spectrometer (Magritek, New Zealand) equipped with a cylindrical 1 T Halbach magnet array, providing a ¹H NMR frequency of 43 MHz. The measurements were carried out at the default spectrometer temperature of 301 K. Before analysis, all samples were allowed to reach thermal equilibrium with the magnet bore for at least 20 min.

The diffusion of both unrestricted and imbibed *n*-hexane was analyzed using the pulsed gradient stimulated echo (PGSTE) sequence, as depicted in Figure 2. The self-diffusion coefficient of unrestricted *n*-
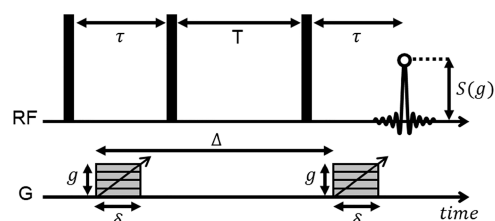
Figure 2. NMR pulse sequence diagram for the pulsed gradient stimulated echo (PGSTE) sequence used in this work. 90° radio frequency (RF axis) pulses are indicated by vertical bars. Gradient pulse timings (G axis) are specified according to the notation of Tanner;[33] magnetic field gradient pulses of incremental magnitude *g* are shown with pulse durations δ, the diffusion observation time is Δ, while *T* and τ represent the longitudinal storage period and spin echo time, respectively (Table S2).

hexane (D_0) was determined by fitting the acquired signal attenuation data at low *b*-factor to[32]

$$\frac{S(g)}{S(0)} = \exp(-bD_0) \tag{1}$$

where $S(0)$ represents the NMR signal in the absence of any applied field gradient, and $S(g)$ is the acquired signal when the magnetic field gradients of magnitude *g* are present (Figure S3). The *b*-factor is given by

$$b = \gamma^2 g^2 \delta^2 \left(\Delta - \frac{\delta}{3}\right) \tag{2}$$
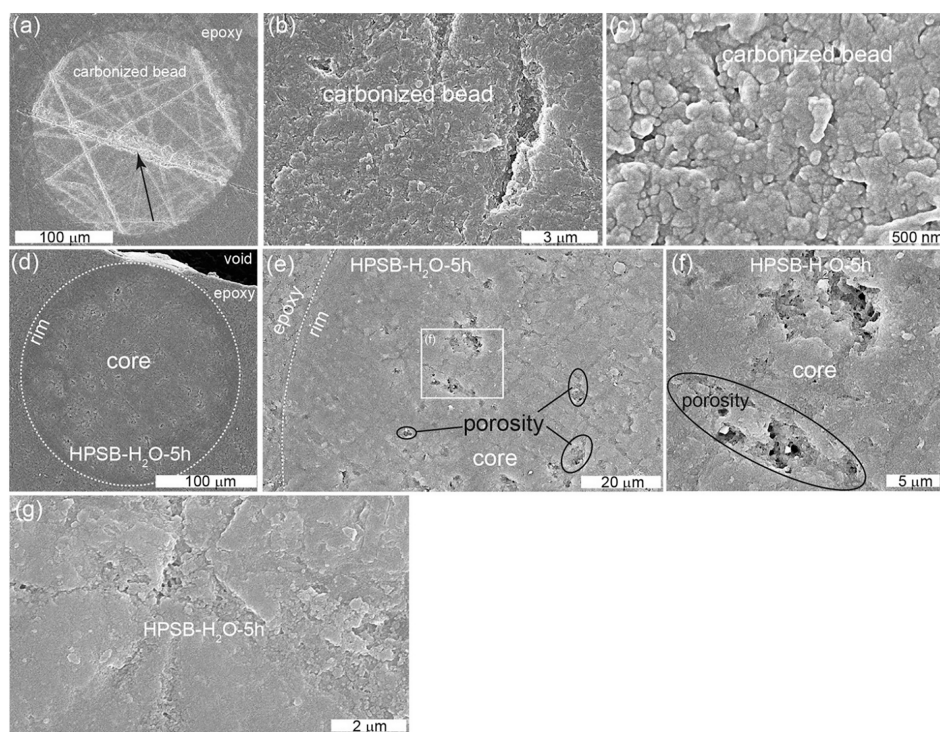
Figure 3. Secondary electron images of cross sections of char (a-c) and sample HPSCB-H$_2$O-5h (d-g). (a) Low-magnification image of spherical char (~393 μm in diameter). Note the numerous polishing scratches (black arrow) preserved in the bead, which document the relative softness of the material in comparison with the surrounding epoxy. (b-c) Higher-resolution image of the globular aggregates of the bead. This morphology is uniform across the entire sphere. (d) Poorly defined rim-core texture in sample HPSCB-H$_2$O-5h. Note the relatively smooth external surface of the rim compared to the porous core. (e,f) Irregularly distributed areas/aggregates of macro- and mesopores of variable size (black ellipses) in the solid core (g). The dotted white line indicates the activated sphere, i.e., the contact between the sphere and epoxy.

where γ is the ^{1}H gyromagnetic ratio, while δ and Δ are the gradient pulse duration and observation time, respectively, as shown in Figure 2. A short Δ time of 20 ms was required to obtain an adequate NMR signal in the presence of very short relaxation times, which arises from the confinement of our n-hexane probe in carbon micropores.

The data collected from samples containing both char and carbon beads immersed in excess n-hexane were fitted using a biexponential equation of the following form[33,34]

$$\frac{S(g)}{S(0)} = p_{inter}\exp(-bD_{inter}) + p_{intra}\exp(-bD_{intra}) \tag{3}$$

where self-diffusion coefficients D_{inter} and D_{intra} describe signal attenuation rates at small (interbead diffusion) and large (intrabead diffusion) b, while p_{inter} and p_{intra} indicate the relative populations characterized by these values. In each case, the measurements were performed by holding the δ constant while linearly varying g.

We calculated the PFG NMR interaction parameter, denoted as η_{intra}, to get further insights into the intrabead n-hexane self-diffusion using the following expression[34]

$$\eta_{intra} = \left. D_0 \middle/ D_{intra} \right. \tag{4}$$

where D_0 is the self-diffusion of n-hexane in the free bulk liquid, which is determined to be $4.29\cdot10^{-9}$ m^2/s from experimental measurements (as is outlined in Figure S3), and the intrabead self-diffusivity of n-hexane is calculated from fitting eq 3 to the experimental data. The details of the parameters used in the PGSTE measurements and the model used for fitting eq 3 can be found in Table S2 and Section 2 of the Supporting Information.

Kinetic Performance of Hierarchical Pore-Structured Carbon Beads. Measurements of the Au recovery from cyanide solutions on HPSCB samples were conducted to examine how the hierarchical pore structures of carbon beads affect the kinetics of adsorption. Coconut shell-based steam-activated carbon (Acticarb GC25PAU, Activated Carbon Technologies Pty Ltd., Australia) was used as an industry benchmark. The Acticarb sample used for comparison was selected to have a size fraction in the range of approximately 351−500 μm. This choice was made to ensure that the granules of Acticarb would be similar in size to those of the produced HPSCBs, facilitating a more meaningful comparison. The carbon was initially ground by using a mortar and pestle and then sieved to obtain the desired size fraction. A gold standard solution with a concentration of 1 g/dm^3 was obtained from PerkinElmer (Glen Waverley, Vic, AUS). High-purity potassium dicyanoaurate(I) (K[Au(Cn)$_2$]), with a purity of 98%, and ACS grade Potassium Cyanide (KCN) were acquired from Sigma-Aldrich (Truganina, Vic, AUS). The measurements using inductively coupled plasma-optical emission spectroscopy (ICP-OES) were conducted using a Thermo Scientific iCAP 7000 series instrument, specifically the model 7600. The ICP-OES spectrometer was operated with the following parameters: RF power, 1150 kW; auxiliary gas (Ar) flow, 0.5 dm^3/min; nebulizer gas (Ar) flow, 0.5 dm^3/min; exposure time, 15 s; orientation, axial only; frequency, 500 Hz; replicates, 3. The wavelengths selected for measuring Au metal ions were 242.795 and 267.595 nm. The 1 g/dm^3 Au standard solution was diluted to concetrations 10, 5, 2, and 1 mg/dm^3, and these solutions were to create the calibration curve. The calibration curve yielded a determination coefficient of 0.999 for both Au wavelengths. The solution matrix used for both the standards and the sample solutions was 0.2% HCl. A stock feed solution of 500.0 mg/dm^3 Au was prepared using 0.7315 g of K[Au(Cn)$_2$] with 12.5 g of KCN and NaOH. The pH of the stock feed was adjusted to 2. This stock feed was used to prepare a 500 cm^3 solution with a concentration of 10.0 mg/dm^3 for each carbon sample. An aggregate of 2 cm^3 was taken from each solution before inserting the carbons and used as a 0 min reference. Approximately 0.125 g of carbon materials wasplaced in a beaker with a magnetic stirrer and maintained at 24 °C. At various time intervals (e.g., 10, 20, 30, 40, 50, 60, 80, 100, 120, 240, 480, 1440, and 2880 min), a 10 cm^3 sample was collected from
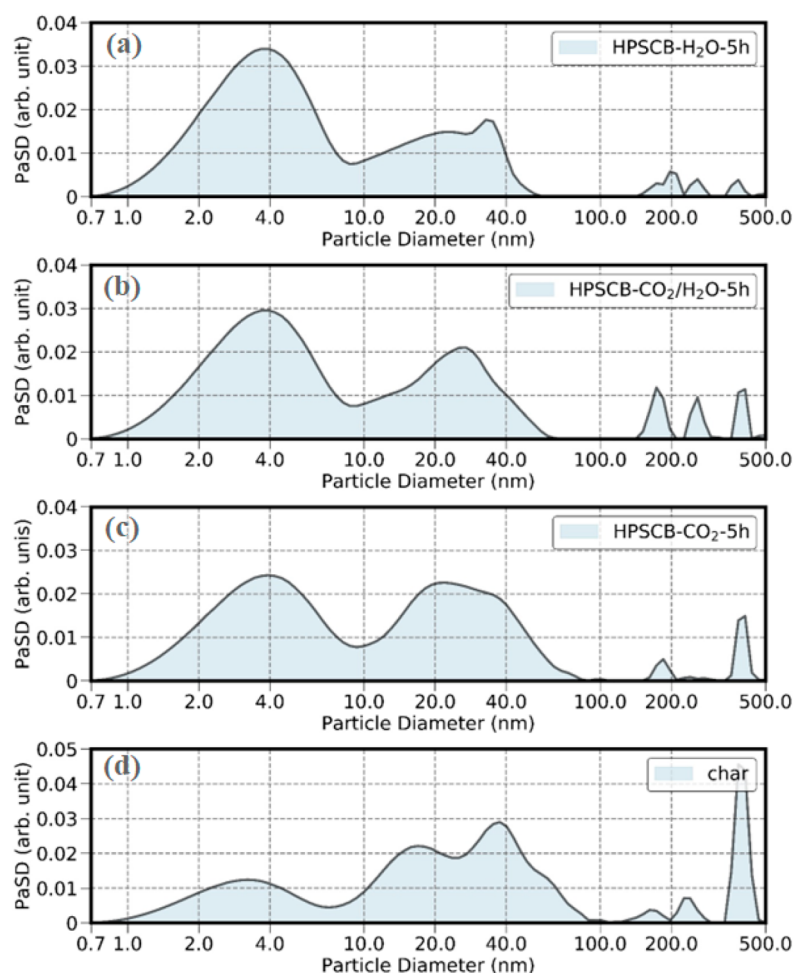
Figure 4. Particle size distributions (PaSD) for HPSCB samples (a-c) activated at 1173 K for 5 h using various activation methods (as outlined in Table 1) and char (d), calculated using SAXS data.

each solution for analysis. Each experimental data point represents averages of three measurements. The average relative standard deviation (RSD) error for the experimental data was less than 1.9%.

The kinetic data acquired from carbon samples were fitted to a pseudo-first-order kinetic model with the following form[35]

$$a(t) = a_e[1 - \exp(-k \cdot t)] \qquad (5)$$

where t is the adsorption time, a_e and $a(t)$ are the adsorption capacity of $Au(CN)_2^-$ on the carbon sample at equilibrium and at time t, respectively, and k is the pseudo-first-order rate constant.

RESULTS AND DISCUSSION

Morphological Changes. The discussion focuses on morphological changes in HPSCB samples activated at 1173 K for 5 h. HPSCBs activated at 1173 K for 3 h exhibit a morphology that closely resembles that of char. Figure 3 displays secondary (SE) and backscattered electron (BSE) images of char and HPSCB-H$_2$O-5h. SEM images collected for HPSCB-CO$_2$-5h, HPSCB-CO$_2$/H$_2$O-5h, and corresponding energy-dispersive X-ray (EDS) spectra are shown in Section 3, Supporting Information (Figures S4−S7). The activation method does not affect the relative concentrations of S, O, and C (e.g., S is ∼2.3 ± 0.3 wt %, the content of O is ∼2.1 ± 0.7 wt %, and C is a dominant element with a relative concentration of ∼95.5 ± 0.6 wt %). Notably, microscopic observations indicate that each of the carbon beads produced exhibited a rim

approximately 10 to 25 μm thick, encircling the core. No rim was detected in the char. Although all carbon beads preserved their external shape, the boundary/interface between the rim and core exhibited variations. HPSCB-CO$_2$-5h and HPSCB-CO$_2$/H$_2$O-5h both exhibited a distinct interface between the rim and the core, whereas the HPSCB-H$_2$O-5h displayed larger embayment areas. Without additional characterization, it is not possible to definitively attribute these embayments to the activation process.

An in-depth analysis of the structural characteristics of the rim and the associated parameters is beyond the scope of this paper. However, it seems imperative to conduct additional research to determine whether there are any differences between the rim and the core. Discrepancies in characteristics such as porosity, density, hardness, or permeability between these two regions hold intriguing potential for modulating adsorption and desorption kinetics.

Figures 4 and S8 illustrate the particle size distribution (PaSD) derived from the SAXS data. These distributions pertain to HPSCB samples activated at 1173 K for 5 (a-c) and 3 h using various activation methods, as well as char (d). Based on the count and locations of the peaks, we can conclude that both char and the produced HPSCB exhibit a distinctive three-level hierarchical structure.[36−40] The initial prominent symmetrical peak at ∼1−10 nm is ascribed to graphene nanoclusters.[36−40] Subsequent WAXS analysis verified the existence of turbostratic

graphene clusters, characterized by an average interlayer distance of $d_{002} = 0.411-0.476$ nm (Table S1 and Figure S2). The second major peak in the range of about 10−50 nm arises from coherent scattering by nanoparticles.[36−40] The ∼10−40 nm peak for HPSCB-H_2O-5h is broadened rather than a symmetrical bell-shaped one (Figure 4). This suggests that the excessive burnoff of char by highly concentrated supercritical steam may lead to a more uniform distribution of nanoparticle sizes. The third level of particulate hierarchy pertains to aggregates of nanoparticles, with sizes that can be accessed via SAXS, reaching up to 500 nm.[36−40] On this level, three peaks were discerned, with char exhibiting the highest intensity and HPSCB-H_2O-5h displaying the lowest. This suggests that the activation method has a relatively minor effect on the structure of nanoparticle aggregates.

Accessible Pore Structure Changes. Figure 5 shows the nitrogen adsorption−desorption isotherms measured at 77 K for
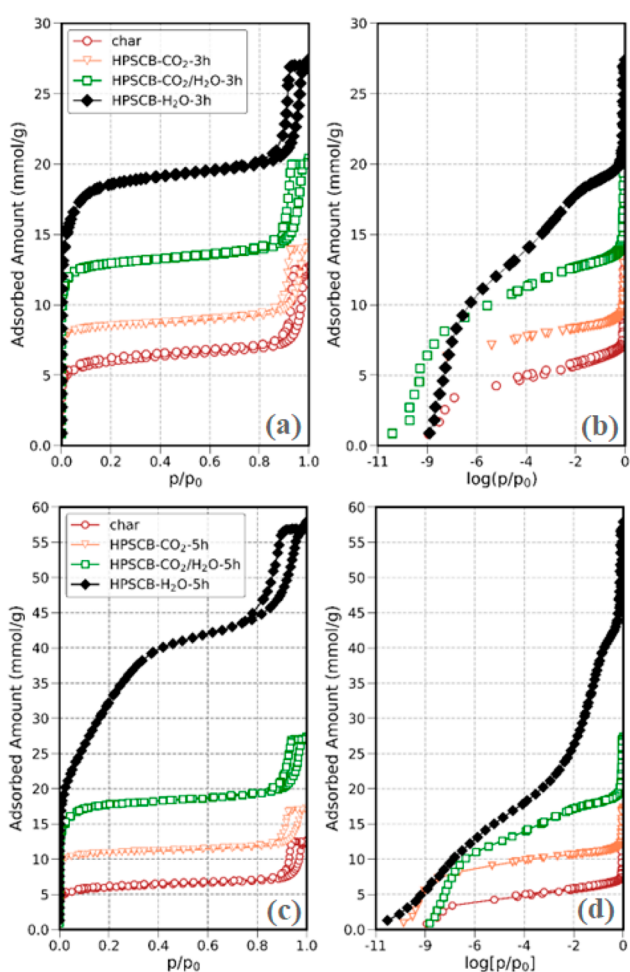
Figure 5. N_2 adsorption−desorption isotherms (77 K) for both char and HPSCB samples activated at 1173 K for 3 and (a, b) 5 h (c, d) using various activation methods (as outlined in Table 1).

char and HPSCBs activated at 1173 K for 3 and (a, b) 5 h (c, d). The N_2 adsorption−desorption isotherms confirm that all samples have a hierarchical structure of a microporous matrix with embedded mesopore channels. Adsorption in micropores (typically smaller 1 nm) at low pressures (p/p_0 < 0.1) is characterized by a sharp concave isotherm of type 1(a),[41] while adsorption in mesopores is characterized by a well-pronounced

hysteresis loop at p/p0 > 0.8. The initial part of the isotherm on the HPSCB-H_2O-3h sample is of type 1(b) that corresponds to carbons with larger micropores and possible narrow mesopores (<2.5 nm). Except for char, the H1-type adsorption−desorption hysteresis loops of similar shape are closed at higher relative pressures with no evidence of cavitation.[41,42] The nitrogen adsorption−desorption isotherms' reproducibility was validated through independent measurements conducted on three separate carbon samples (Figures S9−S11). The adsorption and desorption isotherm for char exhibit partial irreversibility at low pressures, suggesting kinetic limitations in the transport of nitrogen molecules from the exterior to the pores. Additionally, a weak swelling of the char filled with nitrogen is feasible. Detailed examination of the PSD and the contributions of pore volume/ surface area from micro- and mesopores (Figures 6−7 and Table 2) highlights the substantial benefits of USN-assisted activation using highly concentrated supercritical steam. These benefits are particularly evident in terms of the increased accessible surface area and porosity.

The HPSCP-CO_2-3h sample, produced using traditional activation with pure CO_2, is characterized by a sharp PSD with an ultramicropore (<0.7 nm in width) fraction accounting for 93% of the accessible surface area, as indicated in Table 2. The mesopore volume fraction (ranging from 2 to 50 nm in width), at 41 vol % suggests that certain mesopores in the char have been opened by CO_2. The introduction of micrometer-sized water droplets to the CO_2 carrier gas via USN injection leads to significant changes in PSD, as depicted in Figure 6. The primary peak in the PSD at 0.8 nm becomes broader as a result. The majority of the accessible surface area, comprising 78%, can be attributed to supermicropores (ranging from 0.7 to 2.0 nm in width), while the volume fraction of accessible mesopores stands at 38 vol % (Table 2). This increase in the fraction of supermicropores can be explained by the merging of ultra-micropore walls and the simultaneous formation of new supermicropores from the early stages of the activation process.[43,44]

The HPSCB-H_2O-3h sample produced through activation with USN-generated highly concentrated supercritical steam, showcases the highest accessible pore volume (0.88 cm^3/g) and accessible surface area (1272 m^2/g). These values are in line with the highest char burnoff observed after 3 h of activation, as detailed in Table 1. The PSD exhibits a broad peak at 0.9 nm, accompanied by a distinct shoulder at 1.4 nm. Interestingly, the fractions of accessible surface area attributed to ultra-, super-, and mesopores closely resemble those of HPSCB-CO_2/H_2O-3h (Table 2).

As we will demonstrate later, this outcome can be attributed to the relatively short duration of the activation process. Interestingly, extending the time of CO_2 activation from 3 to 5 h does not yield significant changes in the PSD or the corresponding fractions of accessible surface area and accessible pore volume (Figures 6−7 and Table 2). Hence, our conclusion is that the traditional 3 and 5 h of CO_2 activation of char at 1173 K is not sufficient for the alteration of the pore structure. Likewise, there is no significant alteration in the pore structure when extending the activation time from 3 to 5 h for carbon beads produced using CO_2 enriched with USN-generated micron-sized water droplets.

In contrast, subjecting char to 5 h of activation with USN-generated highly concentrated supercritical steam at 1173 K results in a substantial change in the nitrogen adsorption− desorption isotherm, PSD, and accessible surface/volume ratio
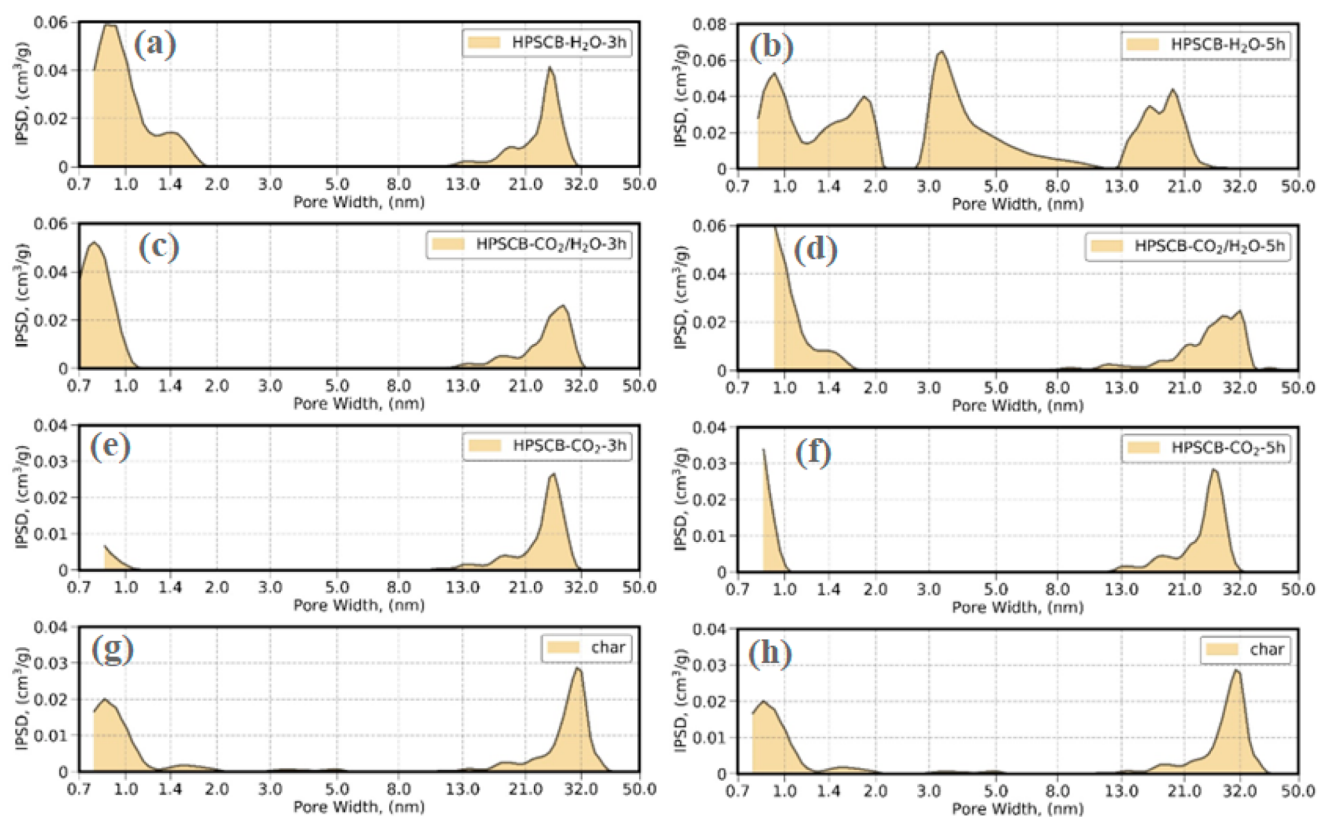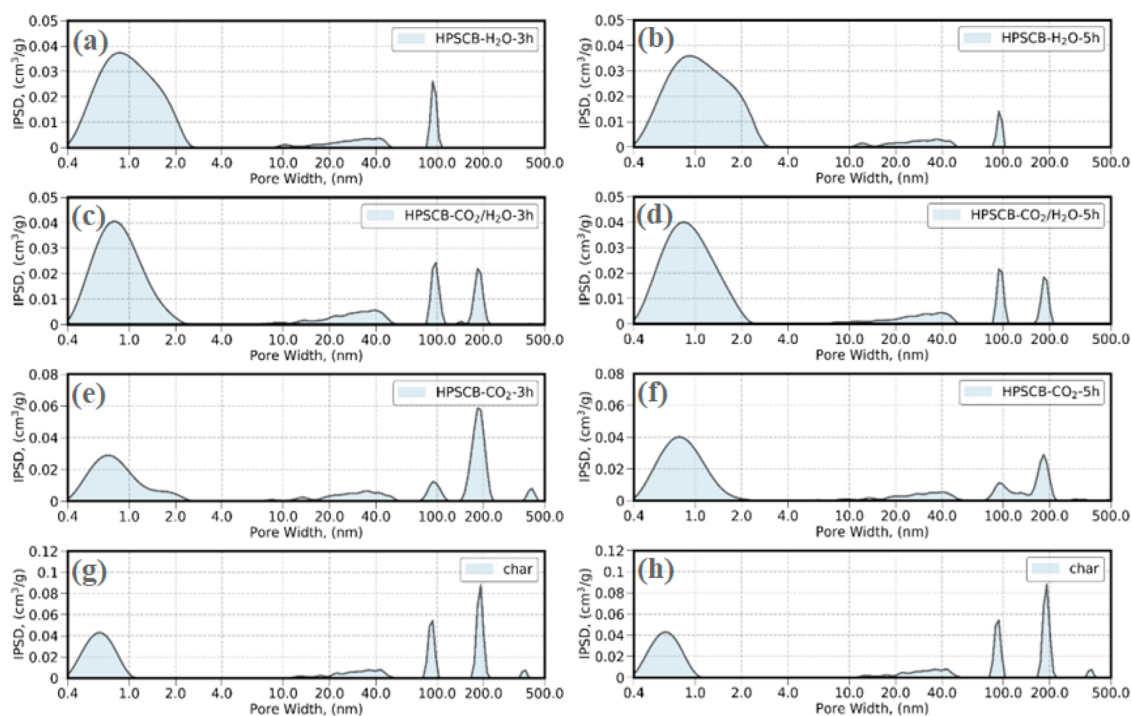
Figure 6. QSDFT pore size distributions for both char and HPSCBs activated at 1173 K for 3 (a, c, e, g) and 5 h (b, d, f, h) using various activation methods (as outlined in Table 1).
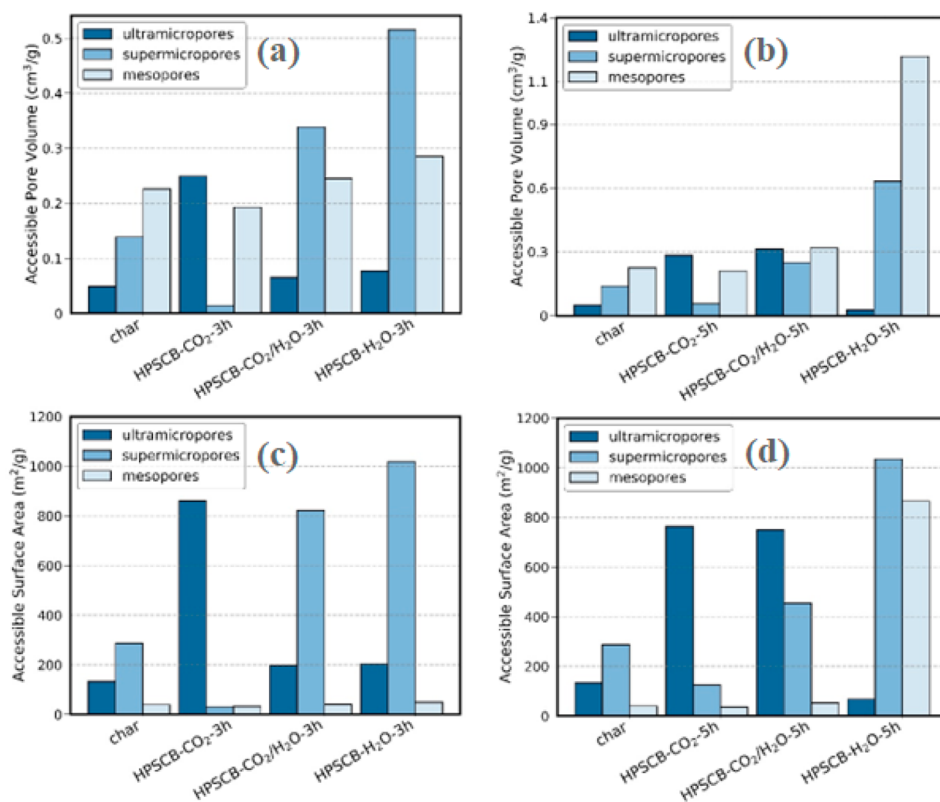
Figure 7. Alterations in the accessible QSDFT ultramicro-, supermicro-, and mesopore volume (a, b) and surface area (c, d) of both char and HPSCB samples activated at 1173 K for 3 (a, c) and 5 h (b, d) using various activation methods (as outlined in Table 1).

Table 2. Evolution of the Accessible Volume and Surface Area (-access), along with the Fractions of Relative Volume and Surface Area Pertaining to Accessible Ultramicropores (-ultra), Supermicropores (-super), and Mesopores (-meso) in Both Char and HPSCB Samples Activated at 1173 K for 3 and 5 h Using Various Activation Methods (as Outlined in Table 1)

Sample	V_{access} (cm^3/g)	$\frac{V_{ultra}}{V_{access}}$ (%)	$\frac{V_{super}}{V_{access}}$ (%)	$\frac{V_{meso}}{V_{access}}$ (%)	S_{access} (m^2/g)	$\frac{S_{ultra}}{S_{access}}$ (%)	$\frac{S_{super}}{S_{access}}$ (%)	$\frac{S_{meso}}{S_{access}}$ (%)
char	0.41	12	34	56	460	29	62	9
HPSCB-CO₂-3h	0.46	54	2	41	923	93	3	4
HPSCB-CO₂/H₂O-3h	0.65	11	52	38	1058	19	78	4
HPSCB-H₂O-3h	**0.88**	**9**	**59**	**33**	**1272**	**16**	**80**	**4**
HPSCB-CO₂-5h	0.55	51	11	38	923	83	13	4
HPSCB-CO₂/H₂O-5h	0.88	35	28	36	1258	60	36	4
HPSCB-H₂O-5h	**1.88**	**2**	**34**	**64**	**1967**	**3**	**53**	**44**

Figure 8. SAXS pore size distributions for both char and HPSCBs activated at 1173 K for 3 (a, c, e, g) and 5 h (b, d, f, h) using various activation methods (as outlined in Table 1).

of ultra-, super-, and mesopores, as evidenced by Figures 6−7 and Table 2. The linear shape of nitrogen adsorption isotherm for HPSCB-H₂O-5h at very low pressures ($\sim10^{-5}$–10^{-3} p/p₀) serves as an indicator of the structural disorder present in the pore walls (Figure 5).[45] The presence of linear segments on the nitrogen adsorption isotherm suggests the organization of pores into clusters. Indeed, the PSD calculated for HPSCB-H₂O-5h reveals the presence of four broad and asymmetric peaks, signifying pore clusters centered at 0.9, 1.8, 3.5, and 18 nm (as shown in Figure 6). The substantial accessible pore volume (1.88 cm³/g) and accessible surface area (1967 m²/g) of HPSCB-H₂O-5h were finely tuned. The majority of the accessible surface area, at 53%, is attributed to supermicropores, followed by a 44% contribution from mesopores, while the contribution from ultramicropores is negligible (Table 2). In terms of accessible volume, mesopores dominate with a 64 vol % contribution, followed by supermicropores at 34 vol %, and a minor 2 vol % contribution from ultramicropores, as shown in Table 2.

Open and Closed Surface Area Changes. The pore size distributions, extracted from SAXS measurements for char and HPSCBs activated at 1173 K for 3 and 5 h using various activation methods (as summarized in Table 1), are presented in Figure 8. In all carbon samples produced, SAXS PSD features a broad peak associated with micropores ($\sim$0.4–3.0 nm) and an asymmetric peak corresponding to mesopores ($\sim$20–40 nm), in agreement with the QSDFT analysis (Figure 6). Furthermore, there are discernible additional contributions from large macropores, ranging from $\sim$100−200 nm in width. Nevertheless, a careful inspection of SAXS PSDs reveals a diminishing relative pore volume associated with these $\sim$100−200 nm macropores as char burnoff progresses. The enlargement and coalescence of these macropores, likely facilitated by enhanced gasification, may account for these observed patterns. It is worth noting that the relative contributions of open (N₂-accessible) and closed (SAXS data) surface areas are contingent upon both time and the chosen activation method, as detailed in Table 3.

The inaccessible surface area of char is notably large, reaching approximately 84%. This high level of inaccessibility is due to the fact that a significant portion of pores is opened during the activation process.[43,44] Traditional activation with CO₂ at 1173 K for 3 to 5 h only manages to open $\sim$39−41% of the total

H

Table 3. Development of Open and Closed Porosity in HPSCBs Activated for 3 and 5 h Using Various Activation Methods (as Outlined in Table 1)[a]

Sample	S_{total} (m²/g)	S_{access} (m²/g)	S_{closed} (%)	S_{open} (%)
char	2843	460	84	16
HPSCB-CO₂-3h	2339	923	61	39
HPSCB-CO₂/H₂O-3h	1841	1058	42	58
HPSCB-H₂O-3h	**1568**	**1272**	**19**	**81**
HPSCB-CO₂-5h	2233	923	59	41
HPSCB-CO₂/H₂O-5h	1483	1258	15	85
HPSCB-H₂O-5h	**2138**	**1967**	**8**	**92**

[a]The values represented include the following: S_{total} - total surface area obtained from SAXS, S_{access} - accessible surface area obtained from QSDFT, and the fractions of closed (S_{closed}) and (S_{open}) surface areas obtained from combined SAXS-QSDFT analysis.

surface area, underscoring the inefficiency of this activation method. The introduction of ultrasonic spraying of micrometer-sized water droplets to CO₂ gas promotes the opening of the closed surface area in char. Following 5 h of activation with CO₂ gas enriched with USN-generated water droplets at 1173 K, approximately 85% of the total surface area becomes accessible. The most impressive results are achieved with USN-generated highly concerted supercritical steam. After 5 h of activation and enhanced gasification of char at 1173 K using this method, the contribution from the accessible surface area increased significantly to 92% (as outlined in Table 3). Notably, this activation process using USN-generated highly concentrated supercritical steam does not require the addition of a chemical activation agent or a carrier gas flow. Moreover, the water consumption is minimal, totaling 12 cm³ per 60 min of activation.

Intrabead Transport Properties Changes. Figure 9 presents the experimental PFG NMR signal attenuation curves of n-hexane-saturated char and HPSCBs activated at 1173 K for 3 (upper panels) and 5 h (bottom panels). Since diffusion rates appear to be sufficiently separated (as shown in the left panels of Figure 9), we utilized two independent straight lines to describe the diffusion data (as expressed in eq 3).[46,47] The initial rapid decay observed is attributed to the unrestricted diffusion of n-hexane, which moves quickly between carbon beads (referred to as interbead diffusion, Table 4).[46] The subsequent portion of the attenuation curve reflects the diffusion of n-hexane confined strictly within the pores (intrabead diffusion, Table 4).[46] It is noteworthy that the uncertainty values for the PFG NMR interaction parameter, obtained from eq 4, exhibit a range from approximately ∼±0.2% to 1.1%.

The reduction in n-hexane self-diffusivity within the pores is attributed to the limited displacement achievable within the confined carbon nanospaces, as opposed to the more unrestricted movement in bulk liquid (η_{intra} > 1, as shown in Figure 9, right panel). The reduced diffusivity of n-hexane can be attributed to several factors, including the tortuosity of the pore network, adsorption interactions occurring at the pore surface, and activated diffusion through pore constrictions.[48] Upon comparing PFG NMR signal attenuation curves for n-hexane in saturated char and HPSCB-CO₂-3h, it becomes evident that the intrabead self-diffusion of n-hexane in these samples is highly similar, as indicated by the η_{intra} values of 9.5−9.7 (Table 4). This observation can be rationalized by the notion that char and HPSCB-CO₂-3h share similar pore structures and pore accessibility characteristics, as detailed in Tables 2 and 3.

Specifically, a short 3-h activation of char with CO₂ at 1173 K does not lead to substantial alterations in the pore network of the char. Ultrasonic spraying of water droplets onto CO₂ gas or directly into the furnace serves to enhance gasification. As a consequence, there is a substantial increase in the accessible porosity, as indicated in Table 2. Hence, self-diffusion of n-hexane within the pores of HPSCB-CO₂/H₂O-3h and HPSCB-H₂O-3h is notably hindered (Figure 9 upper panels). In the case of HPSCB-CO₂/H₂O-3h, the intrabead self-diffusion parameter for n-hexane is notably high at 21.7, suggesting severe restrictions on the self-diffusion of n-hexane molecules within the pores. However, when USN-assisted activation with highly concentrated supercritical steam is utilized, which encourages the development of open porosity with a substantial fraction of accessible surface area and pore volume in the mesopores, the intraparticle intrabead self-diffusion parameter for n-hexane is reduced to 14.5. This reduction indicates an enhanced connectivity of the hierarchical pore network within HPSCB-H₂O-3h compared to HPSCB-CO₂/H₂O-3h.

The extended 5-h activation of char with CO₂ at 1173 K primarily results in the formation of ultramicropores (Table 2 and Figures 6-7). As expected, the intrabead self-diffusion of n-hexane within this sample is considerably impeded, with an interaction parameter of η_{intra} of 23.8. The introduction of water droplets into CO₂ gas via ultrasonic spraying over a 5-h period enhances the self-diffusion of n-hexane within carbon pores, resulting in a reduction of the interaction parameter η_{intra} to 16.7. The highest intrabead diffusivity of n-hexane (η_{intra} = 9.0) was achieved in the HPSCB-H₂O-5h sample, which was produced through a 5-h activation of char with highly concentrated supercritical steam at 1173 K. This result aligns with our expectations, considering the high relative volume fraction of mesopores (64 vol %), moderate volume fraction super-micropores (34 vol %), negligible relative fraction of ultra-micropores (2 vol %), and a very small relative fraction of inaccessible surface area (8%) in the HPSCB-H₂O-5h sample (Table 2). Interestingly, the slopes of the linear segments of our PFG NMR signal attenuation curves, which correspond to intrabead self-diffusion of n-hexane, are remarkably similar for both char and HPSCB-H₂O-5h samples (Figure 9, bottom panels).

The observation that restricted self-diffusion of n-hexane in both char and HPSCB-H₂O-5h pores is quite similar (η_{intra} = 9.5 and 9.0, respectively, as shown in Figure 9) is noteworthy, especially when considering the difference in accessible surface area and accessible pore volume, which are approximately 1507 m²/g and 1.47 cm³/g, respectively (Tables 2 and 3). Additionally, it is worth highlighting that the intrabead self-diffusion coefficient of n-hexane in HPSCB-H₂O-5h (4.7 × 10⁻¹⁰ m²/s) is comparable to the intraparticle self-diffusion coefficients of n-hexane in various porous materials, such as the NaX zeolite crystal (6.4 × 10⁻¹⁰ m²/s),[49] mesoporous silica type MCM-41 with regular 3.8 nm mesopores (4.1 × 10⁻¹⁰ m²/s),[46] and MOF-5 crystal (4.0 × 10⁻¹⁰ m²/s).[50]

Adsorption Kinetic Performance. The PFG NMR intrabead n-hexane self-diffusion data offer valuable insights into the mobility of individual molecules within the pore networks under equilibrium conditions. Our findings have shown that a high relative volume fraction of mesopores enhances the self-diffusion of n-hexane within the pore networks of hierarchically structured carbon beads (Figure 9). Consequently, we anticipate that the hierarchical pore structure of the produced carbon beads could potentially improve the
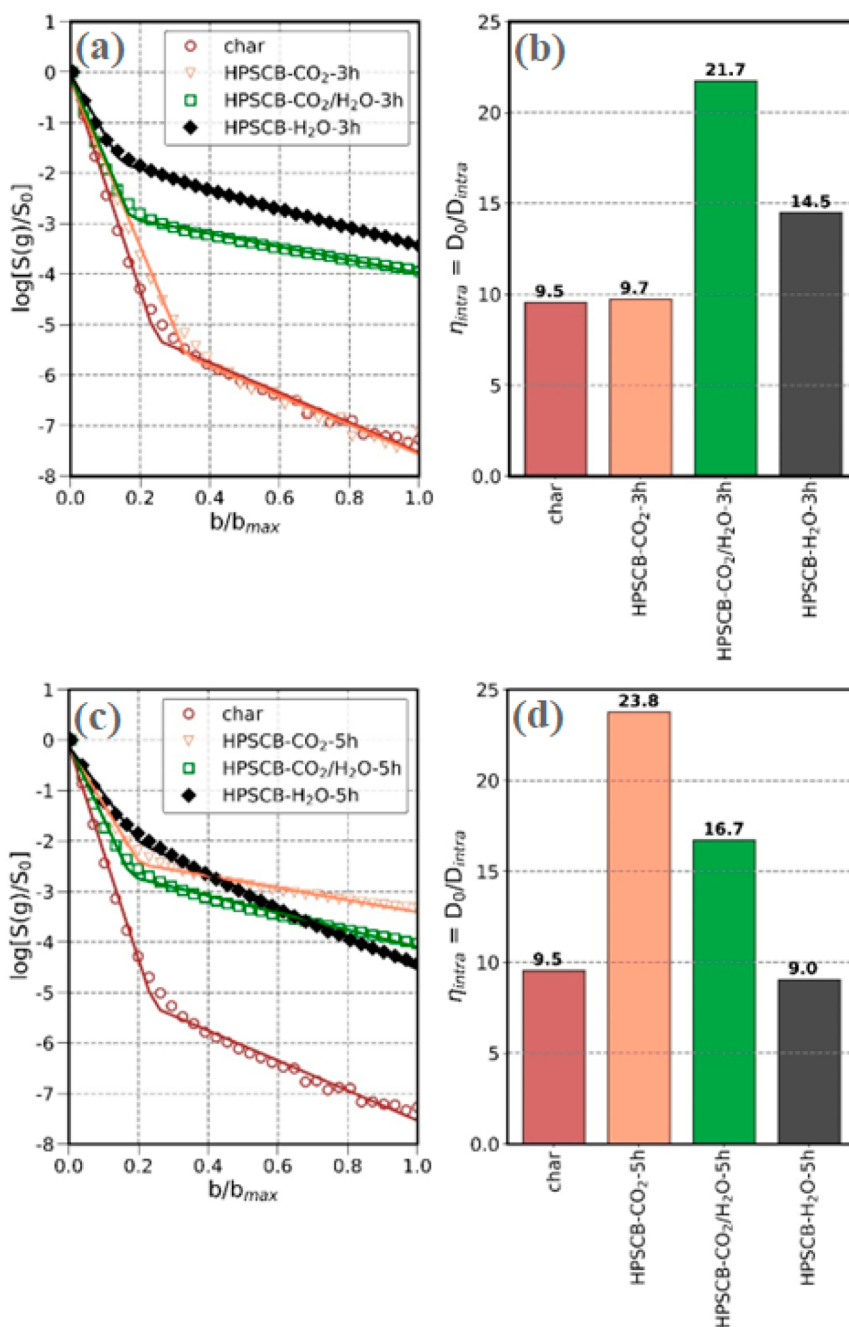
Figure 9. Left panels (a, c) show both the experimental (symbols) and theoretical (solid lines) PFG NMR signal attenuation curves of n-hexane saturated char and HPSCB samples activated at 1173 K for 3 (a, b) and 5 h (c, d) using various activation methods (as outlined Table 1). Right panels (b, d) display the PFG NMR interaction parameter for intrabead n-hexane self-diffusion in the porous networks of the carbon materials that were produced (Table 4).

kinetics of ion adsorption from aqueous solutions. In order to evaluate our hypothesis, we conducted experiments to measure the adsorption of gold from cyanide solutions onto different carbon materials: char, HPSCBs activated at 1173 for 5 h, and the industrial activated carbon Acticarb GC25PAU, which is commonly employed in the carbon-in-pulp process.

HPSCB-H$_2$O-5h exhibits the fastest kinetics of gold adsorption, as evidenced by the pseudo-first-order rate constant of 4.48×10^{-3} 1/min (Figure 10 and Table 5). In contrast, the gold adsorption kinetics in Acticarb GC25PAU is the slowest (k = 2.89×10^{-3} 1/min, Figure 10, and Table 5). This is consistent

with Acticarb GC25PAU having a negligible volume fraction of accessible mesopores (0.5 vol %) and a negligible fraction of accessible surface area of mesopores (0.7%) (Figure S12(a)). Analyzing the experimental results reveals that HPSCB-H$_2$O-5h achieves a 29% and 41% higher gold uptake compared to the benchmark Acticarb GC25PAU activated carbon after 60 and 120 minutes, respectively (Figure 10). Both HPSCB-CO$_2$-5h and HPSCB-CO$_2$/H$_2$O-5h adsorbed the gold cyanide complex faster than did Acticarb GC25PAU activated carbon. This trend aligns with the highly obstructed self-diffusion of n-hexane in Acticarb GC25PAU micropores (η_{intra} = 40.8 obtained from

Table 4. Intrabead (D_{intra}) and Interbead (D_{inter}) Self-Diffusion Coefficients of *n*-Hexane in Char and HPSCBs Activated at 1173 K for 3 and 5 h Using Various Activation Methods (as Outlined Table 1) Obtained from PFG NMR at 301 K[a]

Sample	D_{inter} (m²/s)	D_{intra} (m²/s)	η_{intra}	R^2
char	3.21×10^{-9}	4.50×10^{-10}	9.54	0.9949
HPSCB-CO$_2$-3h	2.49×10^{-9}	4.41×10^{-10}	9.73	0.9942
HPSCB-CO$_2$/H$_2$O-3h	2.49×10^{-9}	1.97×10^{-10}	21.73	0.9939
HPSCB-H$_2$O-3h	$\mathbf{1.85 \times 10^{-9}}$	$\mathbf{2.96 \times 10^{-10}}$	**14.48**	**0.9964**
HPSCB-CO$_2$-5h	1.71×10^{-9}	1.8×10^{-10}	23.76	0.9895
HPSCB-CO$_2$/H$_2$O-5h	2.23×10^{-9}	2.57×10^{-10}	16.71	0.9932
HPSCB-H$_2$O-5h	$\mathbf{1.43 \times 10^{-9}}$	$\mathbf{4.47 \times 10^{-10}}$	**9.05**	**0.9959**

[a]The PFG NMR interaction parameter for intrabead *n*-hexane self-diffusion is computed from eq 4, and R^2 denotes the coefficient of determination.
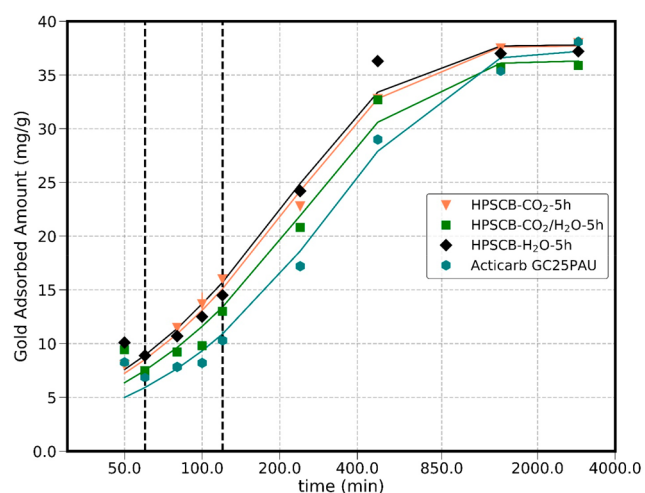
Figure 10. Adsorption kinetics of $Au(CN)_2^-$ on HPSCBs activated at 1173 K for 5 h using various activation methods (as outlined in Table 1) and Acticarb GC25PAU, a commercial activated carbon, measured at pH 2 and 297 K. HPSCB-H$_2$O-5h showed 29% and 41% higher gold uptake than the benchmark Acticarb GC25PAU industrial activated carbon after 60 and 120 min, respectively (dashed lines).

Table 5. Pseudo-First-Order Kinetic Model Coefficients for the Adsorption (pH of 2 and 297 K) of $Au(CN)_2^-$ on HPSCB Samples Activated for 5 h at 1173 K Using Various Activation Methods (as Outlined in Table 1)[a]

Sample	a_e (mg/g)	k (1/min)	R^2
HPSCB-CO$_2$-5h	37.7	4.27×10^{-3}	0.996
HPSCB-CO$_2$/H$_2$O-5h	36.3	3.86×10^{-3}	0.984
HPSCB-H$_2$O-5h	**37.8**	$\mathbf{4.48 \times 10^{-3}}$	**0.985**
Acticarb GC25PAU	37.2	2.89×10^{-3}	0.985

[a]The coefficients for Acticarb GC25PAU, a commercial activated carbon, are also displayed for comparison.

PFG NMR measurements of *n*-hexane saturated Acticarb GC25PAU, Figure S12(b)-(c) in the Supporting Information). Considering the crucial role of gold cyanide complex adsorption kinetics in the carbon-in-pulp process,[26] it is clear that the kinetics of gold adsorption by HPSCBs is highly promising. Columns packed with HPSCB-H$_2$O-5h spherical carbon beads show significant potential for enhancing the

efficiency of gold recovery. This indicates that HPSCB-H$_2$O-5h has the potential to significantly enhance the gold extraction process, making it a valuable asset in gold mining and processing operations.

The Energy Cost of Steam Generation: USN versus the Water Heating Process. Figure 11 illustrates the relationship
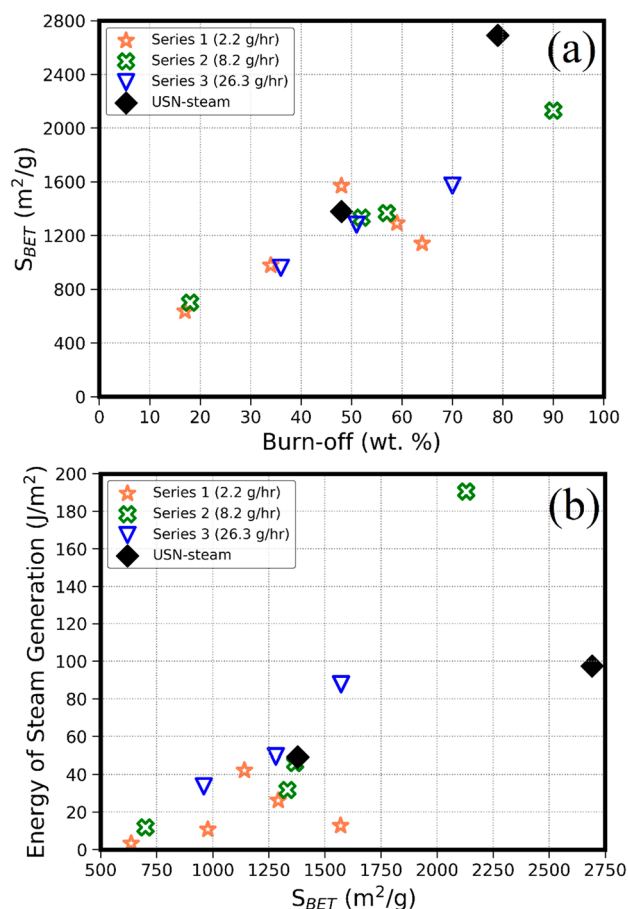
Figure 11. (a) Variation in the apparent BET surface area of activated carbons produced via physical activation with USN and water heating steam generation as a function of burnoff. (b) Energy consumption vs the apparent BET surface area for steam generation via the USN and water heating in the physical activation of char at 1173 K. Steam activation conditions:[51] Set 1: water bath temperature of 333 K, activation temperature 1173 K, and 2.2 g/h steam rate; Set 2: water bath temperature of 353 K, activation temperature 1173 K, and 8.2 g/h steam rate; Set 3: water bath temperature of 363 K, activation temperature 1173 K, and 26.3 g/h steam rate.

between the apparent BET surface area of activated carbons produced through the USN and traditional steam activation at 1173 K, as well as the burnoff degree. In our calculations, we made use of published data pertaining to three series of activated carbons. These activated carbons were produced with varying steam flow rates that originated from the water heating process (Section 4 in the Supporting Information).[51] To maintain consistency when comparing the energy consumption for steam generation estimated from both the current experimental data and previously published results,[51] it is crucial to highlight that all calculations related to the energy cost of steam generation have been standardized per square meter of the apparent BET surface area. One of the primary conclusions drawn from our analysis is that carbon beads, which undergo a 5-h activation

process using USN-generated highly concentrated supercritical steam at 1173 K, exhibit the highest apparent BET surface area, measuring 2691 m^2/g. This level of surface area is achieved at a burnoff degree of approximately 79 ± 11 wt % (Figure 11(a)). The produced spherical carbon beads, averaging 238 ± 1.4 μm in diameter, exhibit mechanical stability (Table S1). The activated carbon, resulting from 6 h of traditional steam activation at 1173 K, achieves its highest apparent BET surface area of 2130 m^2/g at a burnoff of 90 wt % (Figure 11(a)). It is important to note that this activated carbon is in powder form, attributed to the disintegration of carbon beads, as reported by the authors.[51]

The energy cost of USN and water heating steam generation for producing high surface area activated carbons (S_{BET} > ~2000 m^2/g) at 1173 K varies significantly. The estimated energy required for USN steam generation to develop the 1 m^2 apparent BET surface area for HPSCB-H$_2$O-5h is 97 J. On the other hand, the estimated energy required for water heating steam generation to develop the 1 m^2 apparent BET surface area for powdered activated carbon with S_{BET} = 2130 m^2/g is 190 J (Figure 11(b)). For activated carbons with S_{BET} around 1000−1600 m^2/g, the energy cost of both USN and water heating steam generation is similar, approximately ranging from 30 to 50 J/m^2. This is evident from the cluster of experimental points shown in Figure 11(b). These findings consistently demonstrate that the combustion kinetics and reaction pathways between the carbon structure and steam at 1173 K are influenced by the method of steam generation, particularly when the burnoff of char is high, surpassing approximately 70 wt % as illustrated in Figure 11.

CONCLUSIONS

We developed an ultrasonic spray nozzle-quartz tube reactor to produce hierarchical pore-structured carbon beads (HPSCBs). Our innovative approach offers several advantages, including increased energy efficiency per square meter of the apparent BET surface area, reduced activation time and water consumption, and improved gold recovery kinetics when compared to the industrial benchmark. In particular, the production of high surface area HPSCBs (S_{BET} > ~2000 m^2/g) using USN-generated highly concentrated supercritical steam consumes approximately 97 J/m^2 for steam generation. In contrast, the estimated energy cost of steam generation using traditional steam activation is ~190 J/m^2.

Our study demonstrated that 5 h of activation with USN-generated highly concentrated supercritical steam at 1173 K outperforms traditional steam activation. In a previous study,[51] which used traditional steam activation at the same temperature (1173 K), the maximum apparent BET surface area achieved was 2130 m^2/g. However, this process resulted in the breakdown of spherical carbon beads, producing an activated carbon powder. In comparison, our innovative reactor design allowed us to produce the HPSCB-H$_2$O-5h sample with an increased apparent BET surface area of 2691 m^2/g, requiring 1 h less of activation time, and preserving the structural integrity of the carbon beads, indicating superior mechanical stability.

Pulse field gradient NMR revealed that the HPSCB-H$_2$O-5h sample exhibits the fastest intrabead self-diffusivity of n-hexane at 301 K (η_{intra} = 9.0) compared to all other carbon samples, indicating that supermicro- and mesopore clusters are well-connected. The intrabead self-diffusion of n-hexane in HPSCB-H$_2$O-5h (4.7×10^{-10} m^2/s) is comparable with intraparticle self-diffusion of n-hexane in the NaX zeolite crystal (6.4×10^{-10} m^2/

s),[49] mesoporous silica type MCM-41 with regular 3.8 nm mesopores (4.1×10^{-10} m^2/s),[46] and MOF-5 crystal (4.0×10^{-10} m^2/s).[50] The exceptional intrabead self-diffusion rate of n-hexane in the HPSCB-H2O-5h sample can be attributed to its distinct hierarchical pore structure, which predominantly comprises supermicropores (accessible surface area 53%, accessible pore volume 34 vol %, Table 2) and mesopores (accessible surface area 44%, accessible pore volume 64 vol %, Table 2). The intrabead self-diffusion of n-hexane in char (4.5×10^{-10} m^2/s) is slightly higher compared to HPSCB-H2O-5h, yet it remains notably rapid. This experimental result can be attributed to the observation that the hierarchical structure of char consists of a low fraction of ultramicropores (with an accessible surface area of 29% and an accessible pore volume of 12 vol %, as presented in Table 2). Furthermore, since approximately 84% of the total surface area is closed, we anticipate that all accessible pores are distributed around the char's surface, which may enhance the self-diffusion of n-hexane. To further investigate and confirm our hypothesis, additional PFG-NMR research employing different probes is necessary.

The kinetic measurements of gold dicyanide recovery clearly demonstrated that HPSCB-H$_2$O-5h, characterized by interconnected supermicroporous and mesoporous regions, is a superior carbon adsorbent. HPSCB-H$_2$O-5h showed a 29% and 41% higher gold uptake than the benchmark Acticarb GC25PAU industrial activated carbon after 60 and 120 min. This underscores the enhanced adsorption kinetics and efficiency of HPSCB-H$_2$O-5h, making it a promising material for gold recovery applications.

The implementation of USN-assisted steam activation has led to a noteworthy decrease in energy demands, allowing for the production of high-quality carbon beads in a shorter time. The development of highly concentrated supercritical steam activation presents an exciting prospect for the sustainable fabrication of tailored activated carbon featuring adjustable hierarchical pore architectures and remarkably large surface areas.

ASSOCIATED CONTENT

ⓢ Supporting Information

The Supporting Information is available free of charge at https://pubs.acs.org/doi/10.1021/acssuschemeng.3c04171.

Small-angle X-ray spectrum (SAXS) data treatment for analysis of pore and particle size distributions, SAXS diffraction patterns, X-ray diffraction angle (XRD) patterns, description of the procedures for collecting and processing pulse-field gradient nuclear magnetic resonance (PFG NMR) data, scanning electron microscopy (SEM) images, energy dispersive X-ray spectroscopy (EDX) analysis, particle size distributions (PaSD) for char and HPSCB samples activated for 3 h at 1173 K, N$_2$ adsorption−desorption isotherms at 77 K, PFG NMR experimental results for Acticarb GC25PAU activated carbon, distributions of bead sizes obtained from optical microscopy, energy calculation for ultrasonic nozzle steam generation (PDF)

Video depicting the process of ultrasonic spraying of water droplets into the quartz tube reactor (MP4)

Video depicting the process of ultrasonic spraying of water droplets into the quartz tube reactor (MP4)

Video depicting the process of ultrasonic spraying of water droplets into the quartz tube reactor (MP4)

Video depicting the process of ultrasonic spraying of water droplets into the quartz tube reactor (MP4)

AUTHOR INFORMATION

Corresponding Author

Piotr Kowalczyk − *School of Mathematics, Statistics, Chemistry, and Physics, Murdoch University, Murdoch, Western Australia 6150, Australia;* ⓘ orcid.org/0000-0002-7523-0906; Phone: +61 8 9360 6936; Email: P.Kowalczyk@murdoch.edu.au

Authors

Michael Hough − *School of Mathematics, Statistics, Chemistry, and Physics, Murdoch University, Murdoch, Western Australia 6150, Australia*

Artur Deditius − *School of Mathematics, Statistics, Chemistry, and Physics, Murdoch University, Murdoch, Western Australia 6150, Australia; School of Earth Sciences, The University of Western Australia, Perth, Western Australia 6009, Australia*

Neil Robinson − *Department of Chemical Engineering, The University of Western Australia, Perth, Western Australia 6009, Australia;* ⓘ orcid.org/0000-0002-0893-2190

Gerd Elmar Schröder-Turk − *School of Mathematics, Statistics, Chemistry, and Physics, Murdoch University, Murdoch, Western Australia 6150, Australia; Department of Materials Physics, Australian National University, Canberra, Australian Capital Territory 2601, Australia*

Jacob Judas Kain Kirkensgaard − *Department of Food Science, University of Copenhagen, 1958 Frederiksberg, Denmark; Niels Bohr Institute, University of Copenhagen, 2100 Copenhagen, Denmark;* ⓘ orcid.org/0000-0001-6265-0314

Volodymyr M. Gun'ko − *Chuiko Institute of Surface Chemistry, 03164 Kyiv, Ukraine;* ⓘ orcid.org/0000-0001-6333-3441

Alexander V. Neimark − *Department of Chemical and Biochemical Engineering, Rutgers, The State University of New Jersey, Piscataway, New Jersey 08854-8058, United States;* ⓘ orcid.org/0000-0002-3443-0389

Katsumi Kaneko − *Research Initiative for Supra-Materials, Shinshu University, Nagano 380-8553, Japan;* ⓘ orcid.org/0000-0002-2378-478X

Complete contact information is available at:
https://pubs.acs.org/10.1021/acssuschemeng.3c04171

Author Contributions

The manuscript was written through contributions of all authors. All authors have given approval to the final version of the manuscript. **Michael Hough:** Conceptualization, Investigation, Methodology, Data curation, Software, Funding acquisition. **Artur Deditius:** Methodology, Data curation. **Neil Robinson:** Investigation, Methodology, Data curation. **Gerd Elmar Schröder-Turk:** Conceptualization, Data curation. **Jacob Judas Kain Kirkensgaard:** Investigation, Methodology, Data curation. **Volodymyr M. Gun'ko:** Methodology, Software, Data curation. **Alexander V. Neimark:** Software, Data curation. **Katsumi Kaneko:** Data curation. **Piotr Kowalczyk:** Project administration, Conceptualization, Data curation.

Notes

The authors declare no competing financial interest.

REFERENCES

(1) Bandosz, T. J., Ed.; *Activated Carbon Surfaces in Environmental Remediation*; Elsevier: Amsterdam, 2006.

(2) Pomerantseva, E.; Bonaccorso, F.; Feng, X.; Cui, Y.; Gogotsi, Y. Energy storage: the future enabled by nanomaterials. *Science* **2019**, *366*, 6468.

(3) Nanaji, K.; Upadhyayula, V.; Rao, T. N.; Anandan, S. Robust, Environmentally Benign Synthesis of Nanoporous Graphene Sheets from Biowaste for Ultrafast Supercapacitor Application. *ACS Sustain. Chem. Eng.* **2019**, *7* (2), 2516−2529.

(4) Ichikawa, T.; Matsuo, T.; Tachikawa, T.; Yamada, T.; Yoshimura, T.; Yoshimura, M.; Takagi, Y.; Sawama, Y.; Sugiyama, J.-I.; Monguchi, Y.; Sajiki, H. Microwave-Mediated Site-Selective Heating of Spherical-Carbon-Bead-Supported Platinum for the Continuous, Efficient Catalytic Dehydrogenative Aromatization of Saturated Cyclic Hydrocarbons. *ACS Sustain. Chem. Eng.* **2019**, *7* (3), 3052−3061.

(5) Suresh, S.; Bandosz, T. J. Removal of formaldehyde on carbon-based materials: A review of the recent approaches and findings. *Carbon* **2018**, *137*, 207−221.

(6) Zhang, En; Fulik, N.; Hao, G.-P.; Zhang, H.-Y.; Kaneko, K.; Borchardt, L.; Brunner, E.; Kaskel, S. An Asymmetric Supercapacitor-Diode (CAPode) for Unidirectional Energy Storage. *Angew. Chem., Int. Ed.* **2019**, *58*, 13060−13065.

(7) Kowalczyk, P.; Holyst, R.; Terrones, M.; Terrones, H. Hydrogen storage in nanoporous carbon materials: myth and facts. *Phys. Chem. Chem. Phys.* **2007**, *9*, 1786−1792.

(8) Wei, L.; Tian, K.; Zhang, X.; Jin, Y.; Shi, T.; Guo, X. 3D Porous Hierarchical Microspheres of Activated Carbon from Nature through Nanotechnology for Electrochemical Double-Layer Capacitors. *ACS Sustain. Chem. Eng.* **2016**, *4* (12), 6463−6472.

(9) Goldfarb, J. L.; Dou, G.; Salari, M.; Grinstaff, M. W. Biomass-Based Fuels and Activated Carbon Electrode Materials: An Integrated Approach to Green Energy Systems. *ACS Sustain. Chem. Eng.* **2017**, *5* (4), 3046−3054.

(10) Kowalczyk, P.; Terzyk, A. P.; Erwardt, P.; Hough, M.; Deditius, A. P.; Gauden, P. A.; Neimark, A. V.; Kaneko, K. Machine learning-assisted design of porous carbons for removing paracetamol from aqueous solutions. *Carbon* **2022**, *198*, 371−381.

(11) Marsh, H.; Rodríguez-Reinoso, F. *Activated Carbon*; Elsevier: Amsterdam, 2006.

(12) Inagaki, M. *New Carbons - Control of Structure and Functions*; Elsevier Science Ltd.: Amsterdam, 2000.

(13) Leng, J.; Wang, Z.; Wang, J.; Wu, H.-H.; Yan, G.; Li, X.; Guo, H.; Liu, Y.; Zhang, Q.; Guo, Z. Advances in nanostructures fabricated via spray pyrolysis and their applications in energy storage and conversion. *Chem. Rev. Soc.* **2019**, *48*, 3015−3072.

(14) Shiflett, M. B.; Foley, H. C. Ultrasonic deposition of high-selectivity nanoporous carbon membranes. *Science* **1999**, *285*, 1902−1904.

(15) Jeong, C.; Ko, H.; Kim, H.-T.; Sun, K.; Kwon, T.-H.; Jeong, H. E.; Park, Y.-B. Bioinspired, high-sensitivity mechanical sensors realized with hexagonal microcolumnar arrays coated with ultrasonic-sprayed single-walled carbon nanotubes. *ACS Appl. Mater. Interfaces* **2020**, *12*, 18813−18822.

(16) Song, Y. L.; Tsai, S. C.; Chen, C. Y.; Tseng, T. K.; Tsai, C. S.; Chen, J. W.; Yao, Y. D. Ultrasonic spray pyrolysis for synthesis of spherical zirconia particles. *J. Am. Chem. Soc.* **2004**, *87*, 1864−1871.

(17) Skrabalak, S. E.; Suslick, K. S. Porous MoS2 synthesized by ultrasonic spray pyrolysis. *J. Am. Chem. Soc.* **2005**, *127*, 9990−9991.

(18) Bang, J. H.; Suslick, K. S. Applications of ultrasound to the synthesis of nanostructured materials. *Adv. Mater.* **2010**, *22*, 1039−1059.

(19) Gadipelli, S.; Howard, C. A.; Guo, J.; Skipper, N. T.; Zhang, H.; Shearing, P. R.; Brett, D. J. L. Superior multifunctional activity of nanoporous carbons with widely tunable porosity: enhanced storage capacities for carbon-dioxide, hydrogen, water, and electric charge. *Adv. Energy Mater.* **2020**, *10*, 1903649.

(20) Bianco, A.; Chen, Y.; Frackowiak, E.; Holzinger, M.; Koratkar, N.; Meunier, V.; Mikhailovsky, S.; Strano, M.; Tascon, J. M. D.; Terrones, M. Carbon science perspective in 2020: Current research and future challenges. *Carbon* **2020**, *161*, 373−391.

(21) Mikhalovsky, S. V.; Sandeman, S. R.; Howell, C. A.; Phillips, G. J.; Nikolaev, V. G. Biomedical applications of carbon adsorbents. In *Novel Carbon Adsorbents*; Tascón, J. M. D., Ed.; Elsevier Ltd.: Oxford, 2012; pp 639−669.

(22) Malik, D. J.; Warwick, G. L.; Mathieson, I.; Hoenich, N. A.; Streat, M. Structured carbon haemoadsorbents for the removal of middle molecular weight toxins. *Carbon* **2005**, *43*, 2317−2329.

(23) Davankov, V.; Pavlova, L.; Tsyurupa, M.; Brady, J.; Balsamo, M.; Yousha, E. Polymeric adsorbent for removing toxic proteins from blood of patients with kidney failure. *J. Chromatogr. B* **2000**, *739*, 73−80.

(24) Melillo, M.; Gun'ko, V. M.; Tennison, S. R.; Mikhalovska, L. I.; Phillips, G. J.; Davies, J. G.; Lloyd, A. W.; Kozynchenko, O. P.; Malik, D. J.; Streat, M.; Mikhalovsky, S. V. Structural characteristics of activated carbons and ibuprofen adsorption affected by bovine serum albumin. *Langmuir* **2004**, *20*, 2837−2851.

(25) Mikhalovsky, S. V. Emerging technologies in extracorporeal treatment: focus on adsorption. *Perfusion* **2003**, *18*, 47−54.

(26) Nicol, M. J.; Fleming, C. A.; Cromberge, G. The absorption of gold cyanide onto activated carbon. I. The kinetics of absorption from pulps. *J. S. Afr. Inst. Min. Metal.* **1984**, *84*, 50−54.

(27) Kowalczyk, P.; Deditius, A.; Ela, W. P.; Wiśniewski, M.; Gauden, P. A.; Terzyk, A. P.; Furmaniak, S.; Wloch, J.; Kaneko, K.; Neimark, A. V. Super-sieving effect in phenol adsorption from aqueous solutions on nanoporous carbon beads. *Carbon* **2018**, *135*, 12−20.

(28) Neimark, A. V.; Lin, Y.; Ravikovitch, P. I.; Thommes, M. Quenched solid density functional theory and pore size analysis of micro-mesoporous carbons. *Carbon* **2009**, *47*, 1617−1628.

(29) Gor, G. Y.; Thommes, M.; Cychosz, K. A.; Neimark, A. V. Quenched solid density functional theory method for characterization of mesoporous carbons by nitrogen adsorption. *Carbon* **2012**, *50*, 1583−1590.

(30) Landers, J.; Gor, GYu; Neimark, A. V. Density functional theory methods for pore structure characterization: Review. *Colloids Surf., A* **2013**, *437*, 3−32.

(31) Warren, B. E. X-ray diffraction in random layer lattices. *Phys. Rev.* **1941**, *59*, 693−698.

(32) Stejskal, E. O.; Tanner, J. E. Spin diffusion measurements: Spin echoes in the presence of a time-dependent field gradient. *J. Chem. Phys.* **1965**, *42*, 288−292.

(33) Tanner, J. E. Use of the Stimulated Echo in NMR Diffusion Studies. *J. Chem. Phys.* **1970**, *52*, 2523−2526.

(34) Price, W. S. *NMR studies of translational motion: principles and applications*; Cambridge University Press: Cambridge, 2009.

(35) Wang, H.; Yuan, X.; Wu, Y.; Huang, H.; Zeng, G.; Liu, Y.; Wang, X.; Lin, N.; Qi, Y. Adsorption characteristics and behaviors of graphene oxide for Zn(II) removal from aqueous solution. *Appl. Surface Sci.* **2013**, *279*, 432−440.

(36) Bansal, R. C.; Donnet, J. B.; Stoeckli, F. *Active Carbon*; Marcel Dekker: New York, 1988.

(37) Gun'ko, V. M.; Meikle, S. T.; Kozynchenko, O. P.; Tennison, S. R.; Ehrburger-Dolle, F.; Morfin, I.; Mikhalovsky, S. V. Comparative characterization of carbon and polymer adsorbents by SAXS and nitrogen adsorption methods. *J. Phys. Chem. C* **2011**, *115*, 10727−10735.

(38) Gun'ko, V. M.; Kozynchenko, O. P.; Tennison, S. R.; Leboda, R.; Skubiszewska-Zięba, J.; Mikhalovsky, S. V. Comparative study of nanopores in activated carbons by HRTEM and adsorption methods. *Carbon* **2012**, *50*, 3146−3153.

(39) Gun'ko, V. M.; Turov, V. V.; Kozynchenko, O. P.; Nikolaev, V. G.; Tennison, S. R.; Meikle, S. T.; Snezhkova, E. A.; Sidorenko, A. S.; Ehrburger-Dolle, F.; Morfin, I.; Klymchuk, D. O.; Mikhalovsky, S. V. Activation and structural and adsorption features of activated carbons with highly developed micro-, meso- and macroporosity. *Adsorption* **2011**, *17*, 453−460.

(40) Tascón, J. M. D., Ed.; *Novel Carbon Adsorbents*; Elsevier: Amsterdam, 2012.

(41) Thommes, M.; Kaneko, K.; Neimark, A. V.; Olivier, J. P.; Rodriguez-Reinoso, F.; Rouquérol, J.; Sing, K. S. W. Physisorption of gases, with special reference to the evaluation of surface area and pore size distribution (IUPAC Technical Report), Pure Appl. *Chem.* **2015**, *87*, 1051−1069.

(42) Ravikovitch, P. I.; Neimark, A. V. Experimental confirmation of different mechanisms of evaporation from ink-bottle type pores: equilibrium, pore blocking, and cavitation. *Langmuir* **2002**, *18*, 9830−9837.

(43) Molina-Sabio, M.; González, M. T.; Rodríguez-Reinoso, F.; Sepúlveda-Escribano, A. Effect of steam and carbon dioxide activation in the micropore size distribution of activated carbon. *Carbon* **1996**, *34*, 505−509.

(44) Rodríguez-Reinoso, F.; Pastor, A. C.; Marsh, H.; Martínez. Preparation of activated carbon cloths from viscous rayon. Part II: physical activation processes. *Carbon* **2000**, *38*, 379−395.

(45) Kowalczyk, P.; Gauden, P. A.; Furmaniak, S.; Terzyk, A. P.; Wiśniewski, M.; Ilnicka, A.; Łukaszewicz, J.; Burian, A.; Wloch, J.; Neimark, A. V. Morphologically disordered pore model for characterization of micro-mesoporous carbons. *Carbon* **2017**, *111*, 358−370.

(46) Adem, Z.; Guenneau, F.; Springuel-Huet, M.-A.; Gédéon, A.; Iapichella, J.; Cacciaguerra, T.; Galarneau, A. Diffusion properties of hexane in pseudomorphic MCM-41 mesoporous silicas explored by Pulsed Field Gradient NMR. *J. Phys. Chem. C* **2012**, *116*, 13749−13759.

(47) Krutyeva, M.; Grinberg, F.; Furtado, F.; Galvosas, P.; Kärger, J.; Silvestre-Albero, A.; Sepulveda-Escribano, A.; Silvestre-Albero, J.; Rodríguez-Reinoso, F. Characterization of carbon materials with the help of NMR methods. *Microporous Mesoporous Mater.* **2009**, *120*, 91−97.

(48) Kärger, J.; Ruthven, D. M.; Theodorou, D. N. *Diffusion in nanoporous materials*; Wiley-VCH: Weinheim, 2012.

(49) Adem, Z.; Guenneau, F.; Springuel-Huet, M.-A.; Gédéon, A. PFG NMR investigation of hydrocarbon diffusion in large NaX zeolite crystals: Effect of internal field gradients on diffusion data. *Microporous Mesoporous Mater.* **2008**, *114*, 337−342.

(50) Stallmach, F.; Gröger, S.; Künzel, V.; Kärger, J.; Yaghi, O. M.; Hesse, M.; Müller, U. NMR studies on the diffusion of hydrocarbons on the metal-organic framework material MOF-5. *Angew. Chem., Int. Ed.* **2006**, *45*, 2123−2126.

(51) Abdallah, W. Production, and characterisation of activated carbon from sulphonated styrene divinylbenzene copolymer. The Middle East Technical University: Ankara, 2004. https://etd.lib.metu.edu.tr/upload/12605498/index.pdf (accessed 2023-12-21).